Journal of Sound and Vibration (2000) **237**(3), 513–533
doi:10.1006/jsvi.2000.3100, available online at http://www.idealibrary.com on IDEAL®

VIBRATION AND STABILITY OF PRETWISTED SPINNING THIN-WALLED COMPOSITE BEAMS FEATURING BENDING–BENDING ELASTIC COUPLING

O. Song and N.-H. Jeong

Mechanical Engineering Department, Chungnam National University, Taejon, 305-764, Korea

AND

L. Librescu

Engineering Science and Mechanics Department, Virginia Polytechnic Institute and State University, Blacksburg, VA 24061, U.S.A.

(*Received* 22 *October* 1999, *and in final form* 15 *May* 2000)

A number of issues related to the modelling, vibration and stability of anisotropic pretwisted beams rotating at constant angular speed about the longitudinal body-axis fixed in the inertial space are investigated. The analysis is carried out in the framework of a refined theory of thin-walled anisotropic composite beams featuring bending–bending elastic coupling, and encompassing a number of non-classical features such as transverse-shear, anisotropy and pretwist. Special attention is paid to the effect of the spinning speed, pretwist angle, axial compressive load and symmetry/non-symmetry of the beam cross-section on natural frequencies and instability of the structural system. Numerical illustrations highlighting their implication on vibration and stability are displayed and pertinent conclusions are outlined.

1. INTRODUCTION

Rotating structures having the axis of rotation parallel to their longitudinal axis (referred to as the spinning axis), are frequently used in various areas of the current technology.

Such structures are found in gas turbines for higher-power aircraft engines, in helicopter drive applications, in space structures such as satellite booms, as well as in the cutting tools used in boring and milling operations (see, e.g., references [1–8]).

Due to the complexity of accelerations acting throughout the system, the analysis of spinning structures differs from that of their non-rotating counterparts, in the sense that, in addition to the accelerations arising from elastic structural deformations, the ones associated with the Coriolis and centripetal effects have also to be accounted for. Another complexity arises when the beam features an initial pretwist. In such a case, additional couplings are induced which can affect the beam response to static and dynamic loads. As a result, the response of pretwisted beams is likely to be more complex than that of beams with zero pretwist.

The study contained in this paper is carried out in the framework of a thin-walled beam structural model experiencing bending–bending elastic coupling and incorporating a number of non-classical effects such as transverse shear, rotatory inertia, Coriolis acceleration, anisotropy of the structure, and pretwist.

0022-460X/00/430513 + 21 $35.00/0

The available body of literature reveals that in the absence of the initial twist, this problem was approached in the framework of the *solid beam model*, (see, e.g., references [8–13]) and of the *cylindrical shell theory*, (see, e.g., references [14–19]). Moreover, with few exceptions, the analysis was done in the context of metallic structures. For an extensive list of publications related to this topic, the reader is referred to reference [20], whereas a comprehensive survey on the literature devoted to pre-twisted rods and solid beams, can be found in reference [21].

To the best of the authors' knowledge, the present study represents the first work investigating the dynamics and stability of spinning structures modelled as pretwisted anisotropic thin-walled beams.

2. CO-ORDINATE SYSTEMS AND BASIC ASSUMPTIONS

The case of straight pretwisted flexible beams of length L spinning about their longitudinal z-axis at a constant rate Ω is considered (see Figure 1(a)). Two sets of

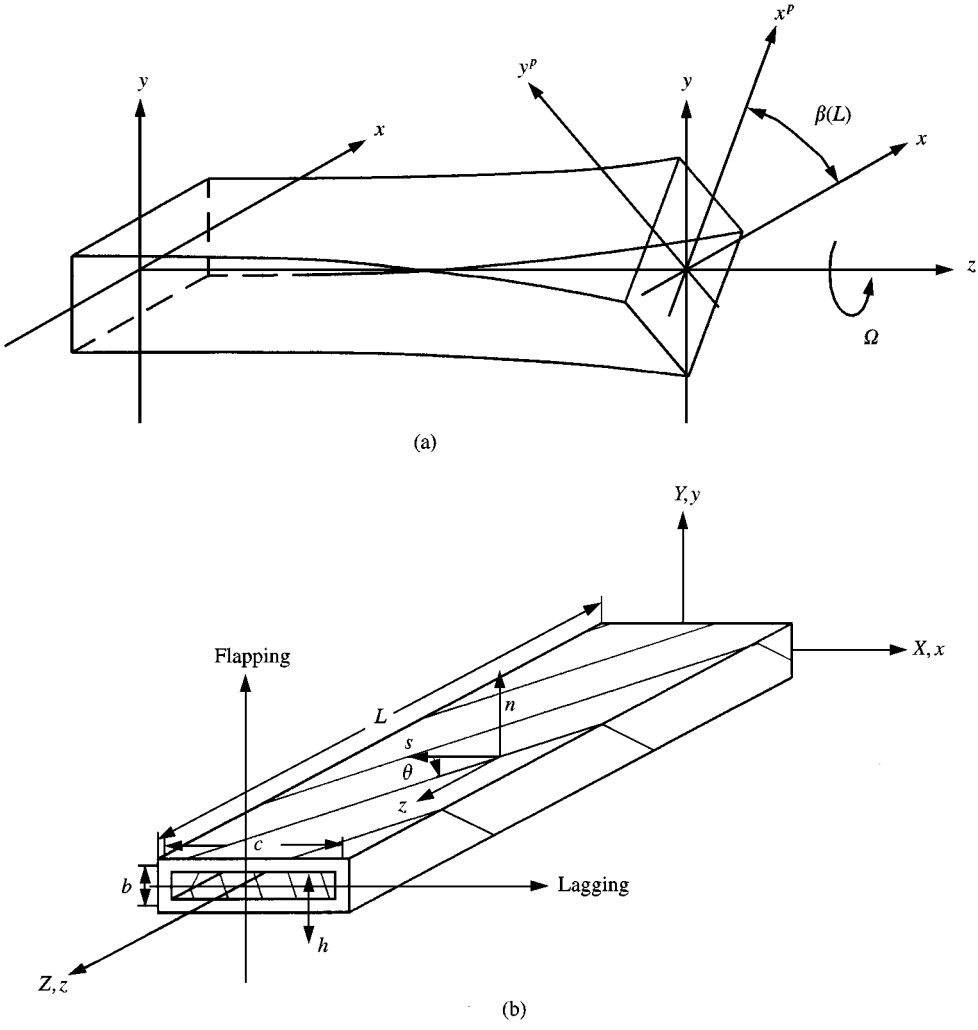

Figure 1. (a) Pretwisted thin-walled beam of closed cross-section. Rotating and inertial co-ordinate systems. (b) Thin-walled beam featuring CUS configuration. (c) Pretwisted beam cross-section. (d) Cross-section of the spinning beam.

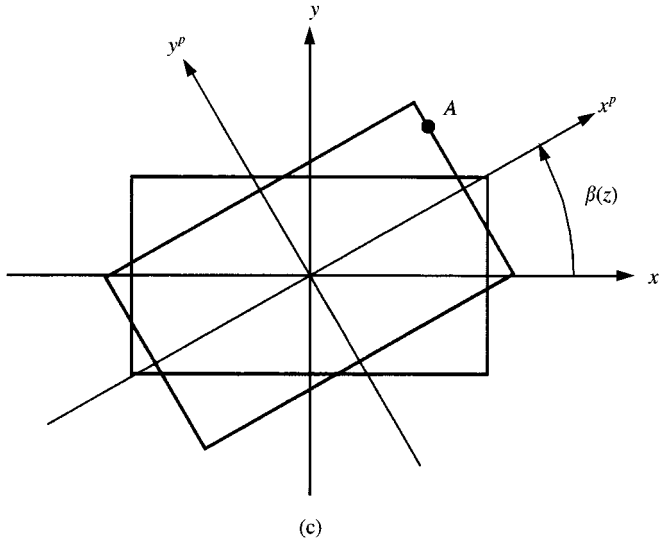

(c)

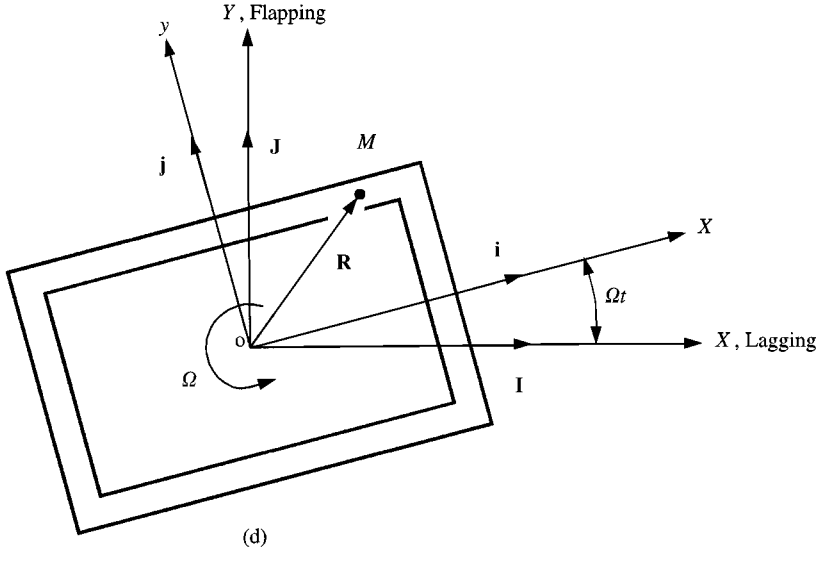

(d)

Figure 1. Continued.

co-ordinates, an inertial one $OXYZ$, and a rotating frame of reference $Oxyz$ with the common origin O, located at the geometric center (coinciding with the elastic center of the beam and with its centroid), are considered (see Figure 1(b)). It is supposed that at $t = 0$, the axes of the two systems coincide while, in the undeformed configuration, the body-fixed and inertial co-ordinates Oz and OZ coincide at any time t. Associated with the co-ordinate systems (x, y, z) and (X, Y, Z), one defines the unit vectors $(\mathbf{i}, \mathbf{j}, \mathbf{k})$ and $(\mathbf{I}, \mathbf{J}, \mathbf{K})$ respectively. In the light of the stipulated assumptions one can represent the spin rate vector $\mathbf{\Omega}$ as $\mathbf{\Omega} = \Omega\mathbf{k}(\equiv \Omega\mathbf{K})$ with $\dot{\mathbf{\Omega}} = 0$.

Besides the co-ordinates (x, y, z), we also define the local co-ordinates (x^p, y^p, z^p), where x^p and y^p denote the principal axes of an arbitrary beam cross-section (see Figure 1(c)).

These two co-ordinate systems are related by the following transformation relationships:

$$x(s, z) = x^p(s)\cos\beta - y^p(s)\sin\beta; \quad y(s, z) = x^p(s)\sin\beta + y^p(s)\cos\beta; \quad z(s) = z^p, \quad \text{(1a, b)}$$

where $\beta(z) = \beta_0 z$, with β_0 denoting the pretwist per unit beam length. From equations (1) it becomes apparent that the systems (x^p, y^p) and (x, y) coincide at the beam root ($z = 0$). It is also appropriate to define here the beam surface co-ordinate system (s, z, n) where s and n are the circumferential and thickness co-ordinates respectively (see Figure 1(d)). The pretwisted beam can be generated by translating a section parallel to itself and preserving the center of mass along the z-axis and at the same time by rotating this section about the z-axis by an angle β proportional to the displacement of the center of mass.

The structural model considered consists of a single-cell thin-walled beam of arbitrary cross-sectional shape. Toward its modelling the following assumptions are adopted: (1) the original cross-section of the beam is preserved, (2) transverse shear effects are incorporated, (3) the constituent material of the structure features anisotropic properties, and, in this context, a special layup inducing the flapwise-chordwise bending coupling is implemented, and finally (4) there is no unbalance, in the sense that the centroidal axis coincides with the axis of rotation.

3. KINEMATICS

In the light of the previously mentioned assumptions, and in order to reduce the three-dimensional (3-D) elasticity problem to an equivalent 1-D one, the components of the displacement vector are represented as (see references [22, 23])

$$u(x, y, z; t) = u_0(z; t) - y(s, z)\phi(z; t), \quad v(x, y, z; t) = v_0(z; t) + x(s, z)\phi(z; t), \quad \text{(2a–c)}$$

$$w(x, y, z; t) = w_0(z; t) + \theta_x(z; t)\left[y(s, z) - n\frac{dx}{ds}\right] + \theta_y(z; t)\left[x(s, z) + n\frac{dy}{ds}\right] - \phi'(z, t)[F_\omega(s; z) + na(s, z)].$$

In these equations $u_0(z; t)$, $v_0(z; t)$, $w_0(z; t)$ denote the rigid-body translations along the x-, y- and z-axis, while $\phi(z; t)$ and $\theta_x(z; t)$, $\theta_y(z, t)$ denote the twist about the z-axis and rotations about the x- and y-axis respectively. The expressions of θ_x and θ_y are

$$\theta_x(z; t) = \gamma_{yz}(z; t) - v_0'(z; t), \quad \theta_y(z; t) = \gamma_{xz}(z; t) - u_0'(z; t). \quad \text{(3a, b)}$$

In equations (2), $F_\omega(s)$ and $na(s)$ play the role of primary and secondary warping functions respectively. For their definition see references [22, 23]. However, having in view that in this analysis the bending–bending coupled motion is considered, only, the terms in equation (2) underscored by an undulated line become immaterial.

It is readily seen that by virtue of equations (2) and (3), the statement of the cross-section non-deformability (implying $\varepsilon_{xx} = 0$; $\varepsilon_{yy} = 0$ and $\gamma_{xy} = 0$ and, consequently, $\varepsilon_{nn} = \varepsilon_{ss} = \gamma_{sn} = 0$), as well as the continuity requirement of w along the mid-line contour (i.e., $\oint(\partial w/\partial s)\,ds = 0$), are fulfilled. It is also seen that in the absence of transverse shear effects

$$\theta_x(z; t) = -v_0'(z; t), \qquad \theta_y(z; t) = -u_0'(z; t), \quad \text{(4a, b)}$$

and in this case, equations (2a–c) are identical to the ones in reference [24]. In these equations, and the forthcoming ones, the primes denote differentiation with respect to the longitudinal z-co-ordinate. The position vector of a point $M(x, y, z)$ belonging to the

deformed structure is

$$\mathbf{R}(x, y, z; t) = (x + u)\mathbf{i} + (y + v)\mathbf{j} + (z + w)\mathbf{k}, \tag{5}$$

where x, y and z are the Cartesian co-ordinates of the points of the continuum in its undeformed state. Recalling that the spin rate was assumed to be constant, the velocity and acceleration of point M are

$$\begin{aligned} \dot{\mathbf{R}} &= [\dot{u} - \Omega(y + v)]\mathbf{i} + [\dot{v} + \Omega(x + u)]\mathbf{j} + \dot{w}\mathbf{k}, \\ \ddot{\mathbf{R}} &= [\ddot{u} - 2\Omega\dot{v} - (x + u)\Omega^2]\mathbf{i} + [\ddot{v} + 2\Omega\dot{u} - (y + v)\Omega^2]\mathbf{j} + \ddot{w}\mathbf{k}, \end{aligned} \tag{6a, b}$$

where the superposed dots denote time derivatives.

4. GOVERNING EQUATIONS

Toward the goal of deriving the equations of motion of spinning beams, and the associated boundary conditions, Hamilton's variational principle is used. This variational principle may be stated as (see, e.g., reference [25])

$$\delta J = \int_{t_0}^{t_1} \left[\delta U - \delta K - \int_{\Omega_\sigma} \underset{\sim}{s}_i \delta v_i \, \mathrm{d}\Omega - \int_\tau \rho H_i \delta v_i \, \mathrm{d}\tau \right] \mathrm{d}t = 0, \tag{7}$$

where

$$U = \frac{1}{2}\int_\tau \sigma_{ij}\varepsilon_{ij}\,\mathrm{d}\tau, \qquad K = \frac{1}{2}\int_\tau \rho(\dot{\mathbf{R}}\cdot\dot{\mathbf{R}})\,\mathrm{d}\tau \tag{8a, b}$$

denote the strain energy functional and the kinetic energy respectively.

In these equations, t_0 and t_1 denote two arbitrary instants of time; $\mathrm{d}\tau (\equiv \mathrm{d}n\,\mathrm{d}s\,\mathrm{d}z)$ denotes the differential volume element; $\underset{\sim}{s}_i (\equiv \underset{\sim}{\sigma}_{ij} n_j)$ denote the prescribed components of the stress vector on a surface element of the undeformed body characterized by the outward normal components n_i; H_i denote the components of the body forces; Ω_σ denotes the external area of the body over which the stresses are prescribed; ρ denotes the mass density; an undertilde sign identifies a prescribed quantity while δ denotes the variation operator. In equations (7) and (8) the Einstein summation convention applies to repeated indices, where Latin indices range from 1 to 3. In the same equations, $(v_1, v_2, v_3) \equiv (u, v, w)$, *and* $(x_1, x_2, x_3) \equiv (x, y, z)$.

In the light of equations (2), (5), (6) and (8) and bearing in mind Hamilton's condition $\delta v_i = 0$ at t_0, t_1, it can readily be shown that

$$\begin{aligned} &\int_{t_0}^{t} \delta K \,\mathrm{d}t \left(\equiv -\int_{t_0}^{t_1} \mathrm{d}t \int_\tau \rho\ddot{\mathbf{R}}\cdot\delta\mathbf{R}\,\mathrm{d}\tau \right) \\ &\quad = -\int_{t_0}^{t_1} \mathrm{d}t \int_\tau [[\ddot{u} - 2\Omega\dot{v} - \Omega^2(x + u)]\delta u + (\ddot{v} + 2\Omega\dot{u} - (y + v)\Omega^2]\delta v + \ddot{w}\delta w]\rho\,\mathrm{d}\tau \\ &\quad = -\int_{t_0}^{t_1} \mathrm{d}t \int_\tau [[\ddot{u}_0 - \underset{\sim\sim}{y\ddot{\phi}} - 2\Omega(\dot{v}_0 + \underset{\sim\sim}{x\dot{\phi}}) - \Omega^2(x + u_0 - \underset{\sim\sim}{y\phi})](\delta u_0 - \underset{\sim\sim}{y\delta\phi}) \\ &\qquad + [\ddot{v}_0 + \underset{\sim\sim}{x\ddot{\phi}} + 2\Omega(\dot{u}_0 - \underset{\sim\sim}{y\dot{\phi}}) - (y + v_0 + \underset{\sim\sim}{x\phi})\Omega^2][\delta v_0 + \underset{\sim\sim}{x\delta\phi}) + \left[\ddot{w}_0 + \left(y - n\frac{\mathrm{d}x}{\mathrm{d}s} \right)\ddot{\theta}_x \right. \\ &\qquad + \left(x + n\frac{\mathrm{d}y}{\mathrm{d}s} \right)\ddot{\theta}_y - \underset{\sim\sim\sim\sim\sim\sim}{\ddot{\phi}'(F_w + na)} \Big] \delta \left[w_0 + \theta_x\left(y - n\frac{\mathrm{d}x}{\mathrm{d}s} \right) + \theta_y\left(x + n\frac{\mathrm{d}y}{\mathrm{d}s} \right) \right. \\ &\qquad \left. - \underset{\sim\sim\sim\sim\sim\sim}{\phi'(F_w + na)} \right] \rho\,\mathrm{d}\tau. \end{aligned} \tag{9}$$

In order to induce the elastic coupling between flapwise-bending and chordwise-bending, a special ply-angle distribution referred to as *circumferentially uniform stiffness* (CUS) configuration achieved by skewing angle plies with respect to the beam axis according to the law $\theta(y) = \theta(-y)$, and $\theta(x) = \theta(-x)$ is implemented. Angle θ denotes the dominant ply-angle orientation in the upper, bottom, and the lateral beam walls measured from the positive s-axis towards the positive z-axis. In this case, based on equations (2) and (3) and the equations expressing the 1-D stress-resultants and stress-couple measures (see reference [22]), from the variational principle (equation (7)), the equations of motion and the boundary conditions involving this type of coupling are obtained. Employment in these equations of constitutive equations, of strain–displacement relationships, and having in view the results in reference [26] related to the inclusion of a longitudinal compressive dead force P, the following *governing equations* are obtained:

$$\begin{aligned}
&\delta u_0\text{: } [a_{43}\theta_x' + a_{44}(u_0' + \theta_y) + a_{45}(v_0' + \theta_x)]' - Pu_0'' = b_1\ddot{u}_0 - \underline{2b_1\Omega\dot{v}_0} - b_1u_0\Omega^2,\\
&\delta v_0\text{: } [a_{52}\theta_y' + a_{55}(v_0' + \theta_x) + a_{45}(u_0' + \theta_y)]' - Pv_0'' = b_1\ddot{v}_0 + \underline{2b_1\Omega\dot{u}_0} - b_1v_0\Omega^2,\\
&\delta\theta_y\text{: } [a_{22}\theta_y' + a_{25}(v_0' + \theta_x) + a_{23}\theta_x']' - a_{44}(u_0' + \theta_y) - a_{43}\theta_x' - a_{45}(v_0' + \theta_x)\\
&\qquad = (b_5 + b_{15})\ddot{\theta}_y + (b_6 - b_{13})\ddot{\theta}_x,\\
&\delta\theta_x\text{: } [a_{33}\theta_x' + a_{23}\theta_y' + a_{34}(u_0' + \theta_y')]' - a_{55}(v_0' + \theta_x) - a_{52}\theta_y' - a_{54}(u_0' + \theta_y)\\
&\qquad = (b_4 + b_{14})\ddot{\theta}_x + (b_6 - b_{13})\ddot{\theta}_y
\end{aligned} \tag{10a–d}$$

and the *boundary conditions at* $z = 0, L$:

$$\begin{aligned}
&\delta u_0\text{: } Q_x = \underset{\sim}{Q}_x \text{ or } u_0 = \underset{\sim}{u}_0,\\
&\delta v_0\text{: } Q_y = \underset{\sim}{Q}_y \text{ or } v_0 = \underset{\sim}{v}_0,\\
&\delta\theta_y\text{: } M_y = \underset{\sim}{M}_y \text{ or } \theta_y = \underset{\sim}{\theta}_y,\\
&\delta\theta_x\text{: } M_x = \underset{\sim}{M}_x \text{ or } \theta_x = \underset{\sim}{\theta}_x.
\end{aligned} \tag{11a–d}$$

Herein $Q_x(z; t)$ and $Q_y(z; t)$ denote the shear forces in the x and y directions, while $M_x(z; t)$ and $M_y(z; t)$ denote the moments about the x- and y-axis respectively. Their definitions can be found in references [22, 23]. In terms of displacement quantities, the static version of homogeneous boundary conditions becomes

$$\begin{aligned}
&\delta u_0\text{: } a_{43}\theta_x' + a_{44}(u_0' + \theta_y) + a_{45}(v_0' + \theta_x) - Pu_0' = 0,\\
&\delta v_0\text{: } a_{52}\theta_y' + a_{55}(v_0' + \theta_x) + a_{45}(u_0' + \theta_y) - Pv_0' = 0,\\
&\delta\theta_y\text{: } a_{22}\theta_y' + a_{25}(v_0' + \theta_y) + a_{23}\theta_x' = 0,\\
&\delta\theta_x\text{: } a_{33}\theta_x' + a_{34}(u_0' + \theta_x) + a_{23}\theta_y' = 0.
\end{aligned} \tag{12a–d}$$

The coefficients $a_{ij} = a_{ji}$ and b_i appearing in these equations as well as in the forthcoming ones denote stiffness and reduced mass terms respectively. Their expressions in terms of their cross-section principal axes (x^p, y^p) counterparts are provided in Appendix A. Equations (10) and (12) reveal that in the context of the ply-angle configuration considered above the flapwise transverse shear is coupled with the chordwise-bending and the chordwise transverse shear is coupled with the flapwise-bending. In addition to the Coriolis acceleration (whose terms are associated with the gyroscopic effect and are underscored by a dotted line), the stiffness quantities a_{45} and a_{23} and the mass terms b_6 and b_{13} which are different from zero only in the case of a pretwisted beam (see Appendix A) induce a supplementary coupling between the bendings in flapping and lagging. However, from the

expressions of a_{45}, a_{23}, b_6 and b_{13}, it can readily seen that for a box-beam of a *square cross-section*, these quantities are zero valued for any value of the pretwist β.

As a result, in such a case, the flapping–lagging coupling arises independently from the pretwist effect, being a result of the considered ply-angle configuration. Consequently, in a buckling analysis of non-spinning pretwisted beams of a *square* cross-section, the buckling response should be independent of the pretwist angle β.

5. THE CASE OF THIN-WALLED BEAMS FEATURING INFINITE TRANSVERSE SHEAR STIFFNESS

Equations (10) and (12) have been obtained for the case of a shearable beam. Towards determining the equations for the non-shearable beam counterpart, elimination of $a_{45}(v_0' + \theta_x)$ and $a_{45}(u_0' + \theta_y)$ in equation (10) and the boundary conditions (12), followed by consideration of $\theta_x \to -v_0'$ and $\theta_y \to -u_0'$, results in *the associated governing equations*

$$\begin{aligned}
\delta u_0\colon\ & [a_{22}u_0'' + a_{23}(v_0'')]'' + Pu_0'' - [(b_6 - b_{13})\ddot{v}_0' \\
& + (b_5 + b_{15})\ddot{u}_0']' + b_1[\ddot{u}_0 - \underline{2\Omega\dot{v}_0} - \Omega^2 u_0] = 0, \\
\delta v_0\colon\ & [a_{33}v_0'' + a_{23}(u_0'')]'' + Pv_0'' - [(b_4 + b_{14})\ddot{v}_0' \\
& + (b_6 + b_{13})\ddot{u}_0']' + b_1[\ddot{u}_0 + \underline{2\Omega\dot{v}_0} - \Omega^2 v_0] = 0,
\end{aligned} \tag{13a, b}$$

and the *boundary conditions*

$$\begin{aligned}
\delta u_0\colon\ & [a_{22}u_0'' + a_{23}(v_0'')]' + Pu_0' - [(b_6 - b_{13})\ddot{v}_0' \\
& + (b_5 + b_{15})\ddot{u}_0' = 0, \text{ or } u_0 = 0, && \text{(14a, b)} \\
\delta v_0\colon\ & [a_{33}v_0'' + a_{23}(u_0'')]' + Pv_0' - [(b_6 - b_{13})\ddot{u}_0' \\
& + (b_4 + b_{14})\ddot{v}_0'] = 0, \text{ or } v_0 = 0, && \text{(14c, d)} \\
\delta u_0'\colon\ & a_{22}u_0'' + a_{23}v_0'' = 0 \text{ or } u_0' = 0, && \text{(14e, f)} \\
\delta v_0'\colon\ & a_{33}v_0'' + a_{23}u_0'' = 0 \text{ or } v_0' = 0, && \text{(14g, h)}
\end{aligned}$$

Similar to the case of shearable beams, also in this case, the flapping–lagging coupling arises via the Coriolis and the pretwist effects.

6. SOLUTION METHODOLOGY OF THE EIGENVALUE PROBLEM OF GYROSCOPIC SYSTEMS

Toward the goal of solving the eigenvalue problem of the gyroscopic system as given by equations (10)–(12) and equations (13) and (14) corresponding to shearable and non-shearable beam structures, respectively, the following steps will be implemented. The first step consists of the representation of displacement functions in the form

$$\begin{aligned}
u_0(z, t) &= \mathbf{U}^{\mathrm{T}}(z)\mathbf{q}_u(t), \qquad v_0(z, t) = \mathbf{V}^{\mathrm{T}}(z)\mathbf{q}_v(t), \\
\theta_x(z, t) &= \mathbf{X}^{\mathrm{T}}(z)\mathbf{q}_X(t), \qquad \theta_y(z, t) = \mathbf{Y}^{\mathrm{T}}(z)\mathbf{q}_Y(t),
\end{aligned} \tag{15a–d}$$

where

$$\begin{aligned}
\mathbf{U} &\equiv [u_1, u_2, \ldots, v_N]^{\mathrm{T}}, \qquad \mathbf{V} \equiv [v_1, v_2, \ldots, v_N]^{\mathrm{T}}, \\
\mathbf{X} &\equiv [X_1, X_2, \ldots, X_N]^{\mathrm{T}}, \quad \mathbf{Y} \equiv [Y_1, Y_2, \ldots, Y_N]^{\mathrm{T}}
\end{aligned} \tag{15e–h}$$

are the vectors of trial functions, while

$$\mathbf{q}_u \equiv [q_1^u, q_2^u, \ldots, q_N^u]^{\mathrm{T}}, \qquad \mathbf{q}_v \equiv [q_1^v, q_2^v, \ldots, q_N^v]^{\mathrm{T}},$$
$$\mathbf{q}_X \equiv [q_1^X, q_2^X, \ldots, q_N^X]^{\mathrm{T}}, \qquad \mathbf{q}_Y \equiv [q_1^Y, q_2^Y, \ldots, q_N^Y]^{\mathrm{T}}, \tag{15i–l}$$

denote the vectors of generalized co-ordinates, while the superscript T denotes the transpose operation. Replacing representations (15) in the variational integral (7), considered in conjunction with equations (8a), (9) and (1), and carrying out the indicated variations and the required integration, result in the equation governing the motion of the gyroscopic system

$$\mathbf{M}\ddot{\mathbf{q}}(t) + \mathbf{G}\dot{\mathbf{q}}(t) + \mathbf{K}\mathbf{q}(t) = 0. \tag{16a}$$

Herein **M** and **K** are the symmetric mass matrix and the stiffness matrix, respectively, **G** is the skew-symmetric gyroscopic matrix, while

$$\mathbf{q}(\equiv [\mathbf{q}_u^{\mathrm{T}}, \mathbf{q}_v^{\mathrm{T}}, \mathbf{q}_X^{\mathrm{T}}, \mathbf{q}_Y^{\mathrm{T}}]^{\mathrm{T}}) \tag{16b}$$

is the overall vector of generalized co-ordinates.

Using the method presented in reference [27], equation (16a) will be expressed in state-space form. In this sense, upon defining the state vector $\mathbf{X} = [\mathbf{q}^{\mathrm{T}}, \dot{\mathbf{q}}^{\mathrm{T}}]^{\mathrm{T}}$ and adjoining the identity $\dot{\mathbf{q}} = \dot{\mathbf{q}}$, equation (16a) is converted to

$$\dot{\mathbf{X}}(\mathbf{t}) = \mathbf{A}\mathbf{X}(t), \tag{17}$$

where the $4N \times 4N$ state matrix **A** is given by

$$\mathbf{A} = \left[\begin{array}{c|c} \mathbf{0} & \mathbf{I} \\ \hline -\mathbf{M}^{-1}\mathbf{K} & -\mathbf{M}^{-1}\mathbf{G} \end{array}\right] \tag{18}$$

while **I** is the unitary matrix. Upon expressing $\mathbf{X}(t)$ in equation (17) as

$$\mathbf{X}(t) = \mathbf{Z}\exp(\lambda t), \tag{19}$$

where **Z** is a constant vector and λ a constant-valued quantity, both generally complex, a standard eigenvalue problem is obtained:

$$(\mathbf{Z} - \lambda\mathbf{I})\mathbf{X} = 0, \tag{20}$$

that can be solved for the eigenvalues λ_r and eigenvectors $\mathbf{X}_r$.

As shown in reference [27], depending upon the positive definiteness, positive semi-definiteness and negative definiteness of the stiffness matrix **K** which contains elements associated with Ω^2, the compressive load and the pretwist angle, the eigenvalues of equation (20) can be respectively: (1) purely imaginary, which implies pure oscillatory motion, the eigenvalues appearing as purely imaginary pairs $\lambda_r = \pm \mathrm{i}\omega_r$ $(r = 1, 2, \ldots, N)$, where ω_r are the rotating (whirling) frequencies; (2) at least one eigenvalue can be zero (which implies divergent motion); or (3) the eigenvalues can be complex conjugate with at least one of these having a positive real part, which implies unstable motion, the instability being of the flutter type. Although this type of instability is typical of non-conservative systems, this can occur also in conservative gyroscopic systems.

7. COMPARISONS WITH AVAILABLE PREDICTIONS

At this point it should be remarked that the equations governing the coupled bending vibrations of pretwisted *thin-walled beam* cantilevers are formally similar to the ones

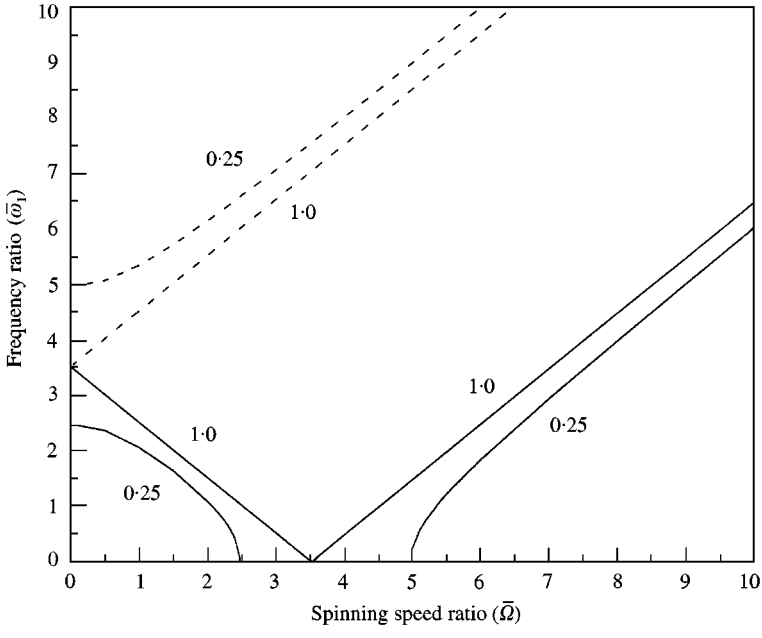

Figure 2. Variation of natural frequency ratios as a function of the dimensionless spin speed for a box-beam of $\mathscr{I}(\equiv a_{33}/a_{22}) = 0{\cdot}25$ and 1 indicated on the graph: $\bar{\omega}_1 = \omega_1/\omega_0$; $\bar{\Omega} = \Omega/\omega_0$; ——, $\bar{\omega}_{IF}$; – – –, $\bar{\omega}_{IB}$.

corresponding to a *solid beam* (see, e.g., references [9, 10]). The difference between these two models reduces to the proper expression of cross-sectional stiffness and mass term quantities. For this reason, the use of dimensionless parameters in which these quantities are absorbed will make it possible to obtain universal results valid for both solid and thin-walled spinning beams. In order to validate both the solution methodology and the structural model developed in this paper, comparisons with a number of results scattered throughout the specialized literature and obtained for solid beams will be presented. One of these results is related to the variation of natural frequency ratios as a function of the spinning speed of an untwisted ($\beta = 0$), and unshearable isotropic beam.

Figure 2 depicts the dependence of rotating frequency $\bar{\omega}_i(\equiv \omega_i/\omega_0)$ as a function of the spin rate $\bar{\Omega}(\equiv \Omega/\omega_0)$, for a beam characterized by the ratio of the principal flexural stiffnesses $\mathscr{I}(\equiv a_{33}/a_{22} = (b/c)^2) = 1$ and 0·25 where $\omega_0^2(\equiv E\sqrt{a_{22}a_{33}}/\rho AL^4)$, A denoting the cross-sectional beam area.

When ($\mathscr{I} = 1$), and $\bar{\Omega} = 0$ the flapping and lagging frequencies in each mode coincide whereas, for $\mathscr{I} = 0{\cdot}25$, the non-rotating bending frequencies in flapping and lagging do not coincide. In the case of $\mathscr{I} = 1$, with the increase of $\bar{\Omega}$, a bifurcation of natural frequencies is experienced, resulting in the upper and lower frequency branches (see references [9, 11]). This reverts to the conclusion that due to the effect of gyroscopic Coriolis forces, two distinct frequency branches of the free bending vibration are produced. The spin rate at which the lowest rotating natural frequency (i.e., the backward whirl frequency) becomes zero-valued is referred to as the critical spinning speed, and corresponds to the divergence instability.

In contrast to the case of a square beam cross-section implying $\mathscr{I} = 1$, when a single critical spinning speed corresponding to each frequency mode number is obtained, in the case of a non-square beam cross-section (for the present case $\mathscr{I} = 0{\cdot}25$), there is a whole

TABLE 1

The first three-mode eigenfrequencies $\bar{\omega}_n (\equiv \omega_n/\omega_0)$*, obtained via various methods, for selected values of the pretwist angle*

Mode no.	Pretwist angle (deg)	Frequency ratio (ω_n/ω_0)					
		Rayleigh–Ritz method [28]	Transformation method [28]	FEM [29]	Bernoulli–Euler FEM [10]	Timoshenko FEM [10]	Timoshenko present
1	30	1·00	1·00	1·00	1·00	1·00	1·00
	60	1·01	1·01	1·01	1·01	1·02	1·01
	90	1·02	1·03	1·02	1·03	1·03	1·03
2	30	5·55	5·56	5·56	5·56	5·57	5·56
	60	4·41	4·43	4·42	4·42	4·43	4·42
	90	3·53	3·55	3·54	3·55	3·57	3·54
3	30	16·12	16·08	16·06	16·06	16·06	16·19
	60	15·02	14·99	14·98	14·99	15·02	14·98
	90	13·58	13·55	13·53	13·53	13·59	13·50

TABLE 2

Frequency ratios for a straight uniform cantilever ($a_{22}/a_{33} = 64$, $L = 35{\cdot}56$ cm)

Mode no.	Ref. [31]			Ref. [32] (FEM)	Present (EGM)
	Standard	Stodola	Experimental		
1	1·00	1·00	1·00	1·00	1·00
2	6·28	6·29	6·09	6·26	6·27
3	17·57	17·74	17·11	17·57	17·55
4	34·38	35·16	33·59	34·60	34·44

domain of critical spinning speeds, bordered by $(\bar{\Omega}_{cr})_1$ and $(\bar{\Omega}_{cr})_2$, for which the dynamic system becomes unstable. Herein $(\bar{\Omega}_{cr})_1$ and $(\bar{\Omega}_{cr})_2$, denote the lower and upper bounds of the divergence instability domain (see Figure 2). The results displayed in Figure 2 coincide with those in references [9, 11] obtained via the use of various numerical procedures.

A further validation of the solution methodology used in this paper concerns the case of free vibration of a pretwisted non-rotating beam of rectangular cross-section characterized by the cross-section ratio $c/b = 16$, $b = 0{\cdot}5$ cm and $L = 100$ cm.

The results displayed in Table 1 compare the normalized frequencies $\bar{\omega}_n (\equiv \omega_n/\omega_0)$ obtained via different numerical procedures, where ω_n are the actual frequencies, and $\omega_0 = 26{\cdot}083$ rad/s is the lowest frequency of the untwisted beam counterpart.

The considered numerical procedures involve the Rayleigh–Ritz and transformation methods [28]; the finite element method (FEM) for the Euler–Bernoulli and Timoshenko beam models [29, 10], as well as the present method for shearable beams. The results obtained for this case reveal that, consistent with the actual characteristics of the beam, the variation of the various mode frequencies with the pretwist angle follows a similar trend to

TABLE 3

Comparison of the buckling coefficients S ($\equiv P_{cr}L^2/a^p_{33}$) obtained via FEM and the present method, for selected values of the pretwist angle β and cross-section aspect-ratio R. Shearable beam model

β (deg)	$R = 1{\cdot}0$		$R = 0{\cdot}75$		$R = 0{\cdot}5$		$R = 0{\cdot}25$	
	Ref. [10]	Present	Ref. [10]	Present	Ref. [10]	Present	Ref. [10]	Present
0	2·453	2·453	2·453	2·453	2·453	2·453	2·453	2·453
90	2·453	2·453	2·562	2·554	2·624	2·649	2·686	2·669
180	2·453	2·453	2·802	2·794	3·106	3·081	3·304	3·273
270	2·453	2·453	2·963	2·953	3·479	3·439	3·857	3·803
360	2·453	2·453	3·004	2·991	3·596	3·539	4·048	3·973

that described in references [30, 31]. On the other hand, a comparison of the results generated via different numerical procedures reveals an excellent agreement.

In Table 2, the comparisons of the theoretical and experimental results obtained in references [31, 32] for a uniform cantilever with the present ones, reveal again an excellent agreement.

A final test case concerns the buckling of a pretwisted shearable beam of $L = 0{\cdot}5$ m and $c = 2$ m. The values of the buckling coefficient $S(\equiv P_{cr}L^2/a^p_{33})$ for selected values of the pretwist angle and cross-section ratios R, predicted via the FEM developed in reference [10], are compared in Table 3 with the present ones, and an excellent agreement is revealed.

8. NUMERICAL SIMULATIONS AND DISCUSSION

A number of cases intended to highlight the effects played by the pretwist and compressive load on the vibration and instability of spinning cantilevered thin-walled beams will be presented.

The numerical simulations involve a box-beam of rectangular cross-section of fixed dimensions indicated in Figure 1(b). The beam is supposed to be manufactured from a graphite-epoxy material whose on-axis elastic properties are $E_L = 30 \times 10^6$ psi ($20{\cdot}68 \times 10^{10}$ N/m^2), $E_T = 0{\cdot}75 \times 10^6$ psi ($5{\cdot}17 \times 10^9$ N/m^2), $G_{LT} = 0{\cdot}37 \times 10^6$ psi ($2{\cdot}55 \times 10^9$ N/m^2), $G_{TT} = 0{\cdot}37 \times 10^6$ psi ($2{\cdot}54 \times 10^9$ N/m^2), $\mu_{TT} = \mu_{LT} = 0{\cdot}25$, $\rho = 14{\cdot}3 \times 10^{-5}$ lb s^2/in^4 (1528·15 N s^2/m^4), where the subscripts L and T denote directions parallel and transverse to the fibers, respectively.

Throughout the numerical illustrations, the case of a clamped–free beam was considered.

In Figure 3, in the absence of the compressive load, the dependence of $\bar{\omega}_1(\equiv \omega_1/\hat{\omega}_1)$ versus the normalized spin rate $\bar{\Omega}(\equiv \Omega/\hat{\omega}_1)$ for a beam without pretwist, for selected values of the beam cross-section parameter $R(\equiv b/c)$ is depicted. Herein, as in the remaining plots, the ply-angle θ was considered to be $\theta = 0^\circ$. The normalizing fundamental frequency $\hat{\omega}_1(= 164{\cdot}73$ rad/s) corresponds to a non-rotating beam of square cross-section, the material being characterized by $\theta = 0^\circ$. For the non-rotating beam, $\bar{\Omega} = 0$, and for the case $R = 1$, the flapping and lagging frequencies coincide.

However, as it appears from Figure 3, and previously revealed in Figure 2, for beams characterized by $R \neq 1$, the non-rotating frequencies in flapping and lagging do not coincide.

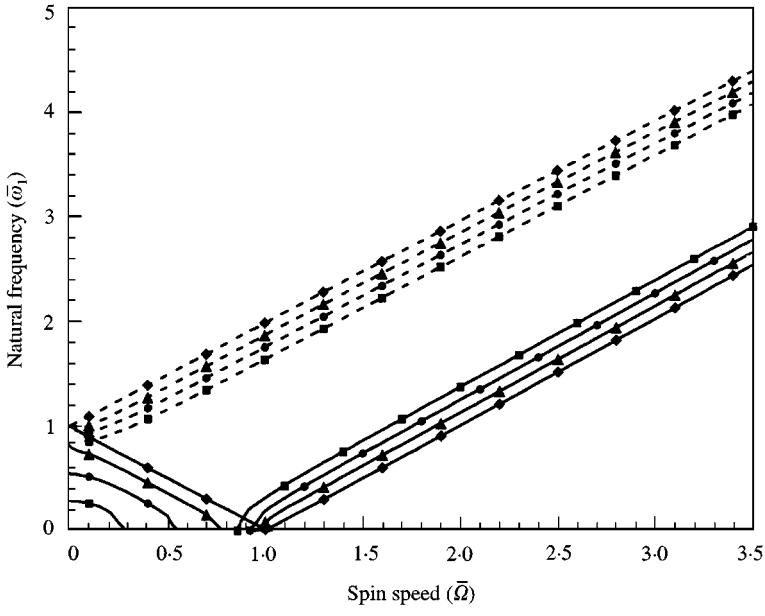

Figure 3. Rotating frequency–spin rate interaction for a beam of selected values of R, $\theta = 0^\circ$ and pretwist angle $\theta = 0^\circ$: ——, $\bar{\omega}_{1F}$; – – –, $\bar{\omega}_{1B}$; ■, $R = 0{\cdot}25$; ●, $R = 0{\cdot}5$; ▲, $R = 0{\cdot}75$; ◆, $R = 1$.

The recorded results reveal again that, in contrast to the case of thin-walled beams of square cross-sections, $R = 1$, in which case a single critical divergence spin speed is experienced, in the case of beams of rectangular cross-sections, $R \neq 1$, there is a whole domain of critical spinning speeds for which the systems becomes unstable by divergence. Moreover, for the beam characterized by $R \neq 1$, for $R < 1$, the domains of spinning speed instability are shifted towards lower spinning speeds.

In Figure 4, the variation of the divergence speed instability domain as a function of the pretwist angle and for selected values of R has been depicted. For selected cross-section ratios R, in this figure the variation of the divergence speed instability domain spanned between the lower and upper bands, $(\bar{\Omega}_{cr})_1$ and $(\bar{\Omega}_{cr})_2$, respectively, versus the pretwist angles, is depicted. From this plot it becomes apparent that for $R = 1$ the spinning divergence speed does not depend on the pretwist angle and, as a result, for this case the critical speed domain reduces to a single critical spin speed. The results emerging from this figure also reveal that for $R < 1$ the divergence speed instability domain decreases as the pretwist angle increases. Similar conclusions have been obtained within the framework of a solid beam model in reference [10], where the FEM was used to generate the results.

In Figure 5 the effect of the pretwist is involved, where the total angle of pretwist at the beam tip is indicated. From this figure it becomes apparent that for the beams characterized by $R \neq 1$, with increase of $\bar{\Omega}$, the lower frequency branch (corresponding to the forward whirl) decreases while the upper mode frequency branch (corresponding to the backward whirl) increases. The spin speed at which the forward whirl frequency becomes zero constitutes the divergence spin speed. Beyond this spin speed the system becomes stable again and with the further increases of $\bar{\Omega}$, for a certain value of $\bar{\Omega} = \bar{\Omega}_{flutter}$, referred to as the flutter spin speed, two eigenfrequencies coalesce. Beyond $\bar{\Omega}_{flutter}$ the two eigenfrequencies becomes complex conjugate. From Figure 5 it clearly appears that for $R = 1$, the flutter spin speed is theoretically infinite and decreases with the decrease of the parameter R.

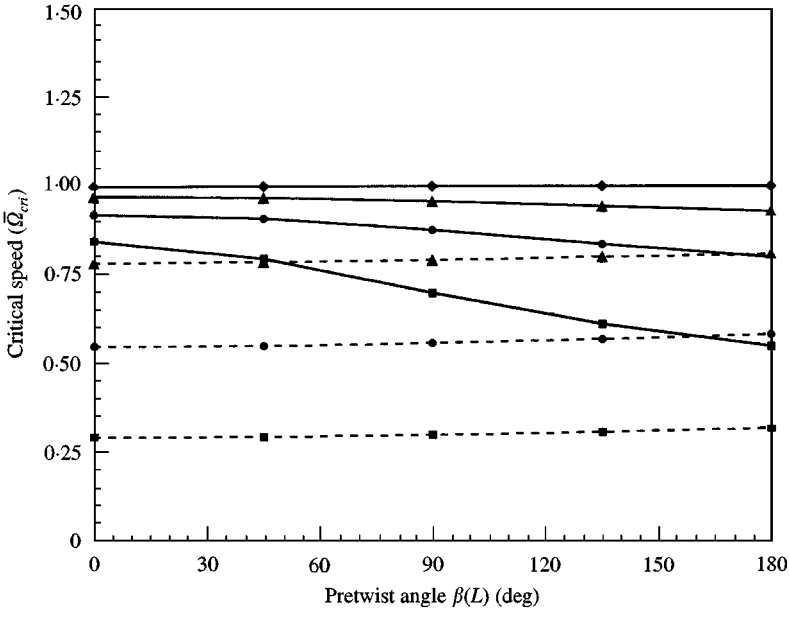

Figure 4. Variation of the critical spin speed in divergence as a function of the pretwist angle for selected values of R and $\theta = 0°$. The divergence instability domain is extended between $(\Omega_{cr})_1$ and $(\Omega_{cr})_2$: – – –, $(\bar{\Omega}_{cr})_1$; ——, $(\bar{\Omega}_{cr})_2$. ■, $R = 0{\cdot}25$; ●, $R = 0{\cdot}5$; ▲, $R = 0{\cdot}75$; ◆, $R = 1$.

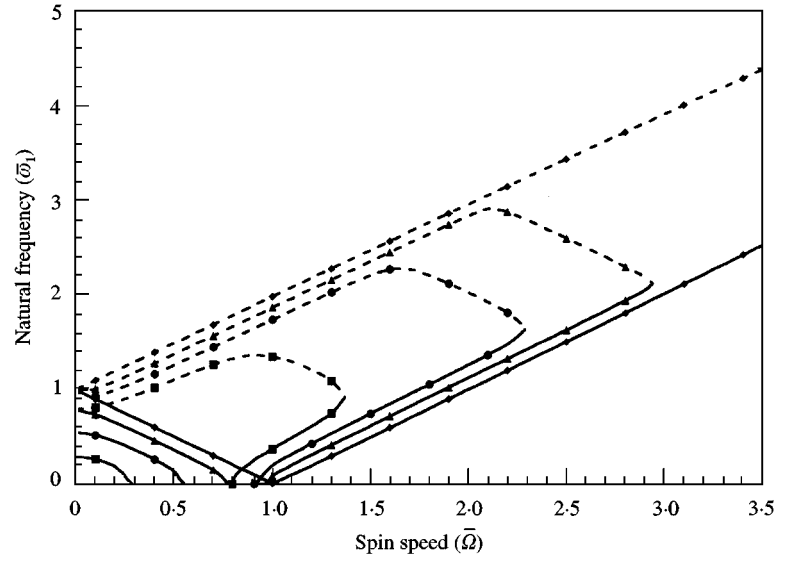

Figure 5. Rotating frequency–spin rate interaction for a beam with selected values of R; $\theta = 0$ and pretwist angle at the beam tip $\beta = 45°$. ——, $\bar{\omega}_{IF}$; – – –, $\bar{\omega}_{1B}$; ■, $R = 0{\cdot}25$; ●, $R = 0{\cdot}5$; ▲, $R = 0{\cdot}75$; ◆, $R = 1$.

Figure 6 records the dependence of $\bar{\omega}_1$ versus $\bar{\Omega}$ for fixed pretwist angle and selected R ratios. In addition to the previously mentioned findings, the results of Figure 5 and 6 reveal that in the case of a *square* cross-section beam, for any pretwist angle and spin speed, the phenomenon of flutter instability does not occur.

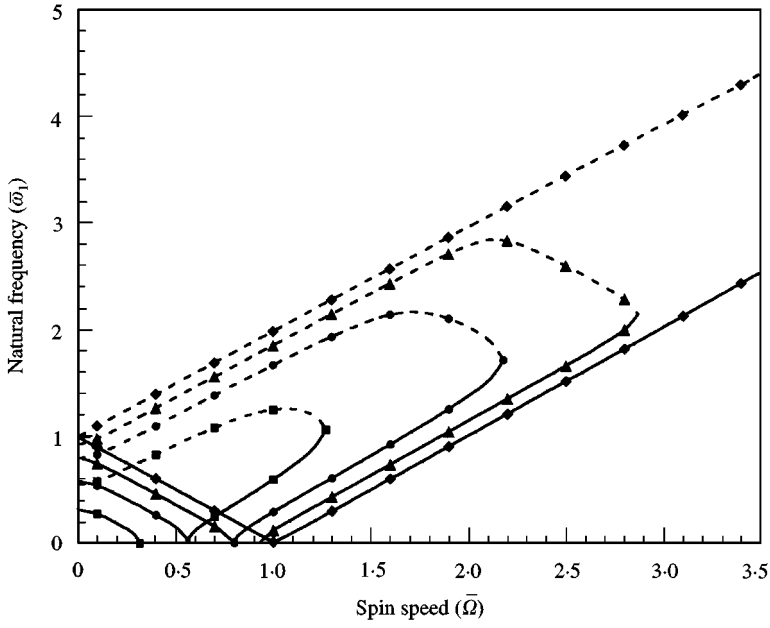

Figure 6. Rotating frequency–spin rate interaction for selected values of beam parameter R, $\theta = 0^\circ$ and the pretwist angle $\beta = 180^\circ$. ——, $\bar{\omega}_{1F}$; – – –, $\bar{\omega}_{1B}$; ■, $R = 0{\cdot}25$; ●, $R = 0{\cdot}5$; ▲, $R = 0{\cdot}75$; ◆, $R = 1$.

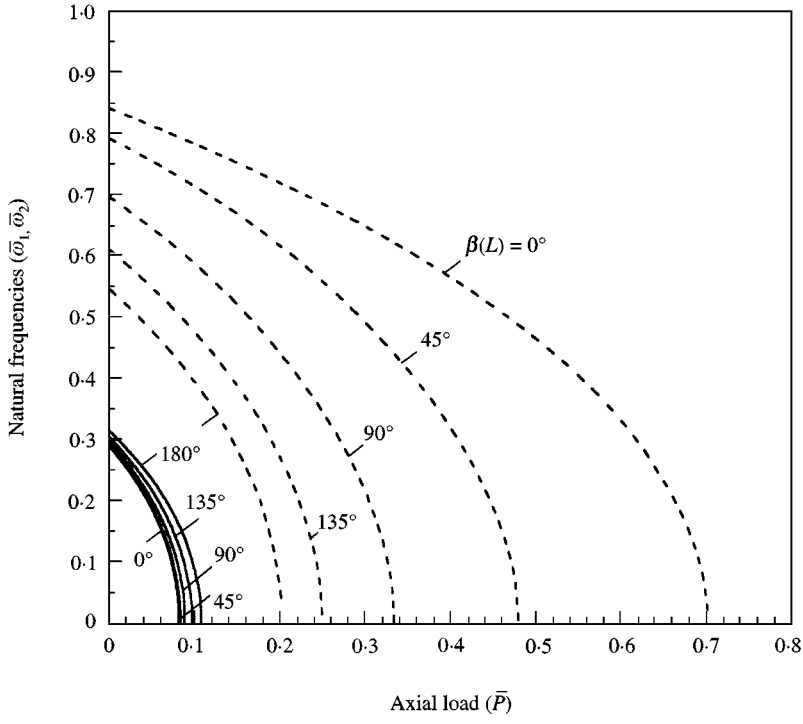

Figure 7. Dependence of the two branches $\bar{\omega}_i$ ($i = 1, 2$) of the fundamental frequency on the axial compressive load $\bar{P}$ for selected values of the pretwist angle β (deg). The considered box-beam is characterized by $R = 0{\cdot}25$, $\theta = 0^\circ$, $\Omega = 0$; ——, $\bar{\omega}_1$; – – –, $\bar{\omega}_2$.

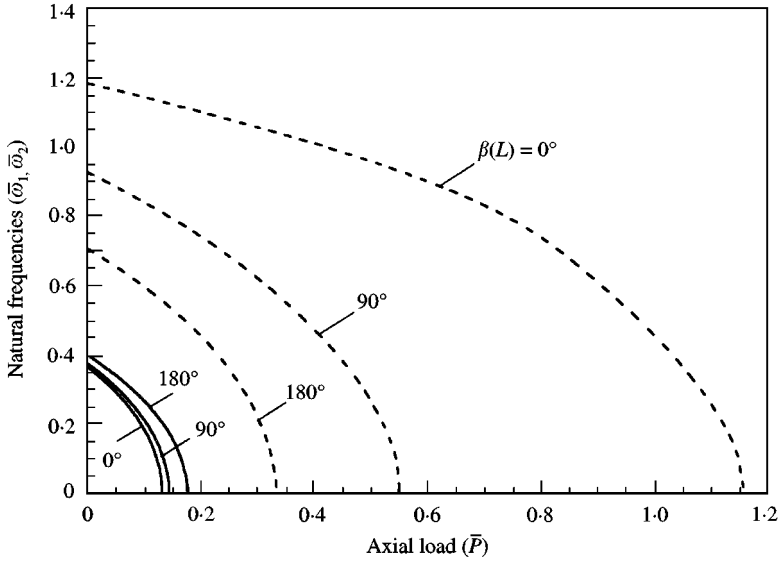

Figure 8. The counterpart of Figure 7 for the ply-angle $\theta = 45°$; ——, $\bar{\omega}_1$; – – –, $\bar{\omega}_2$.

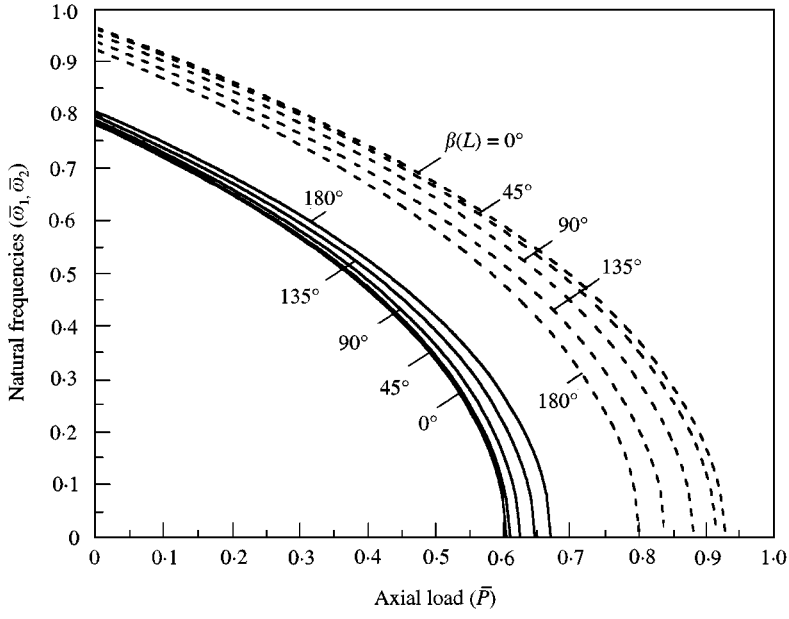

Figure 9. Dependence of the two branches $\bar{\omega}_i$ $(i = 1, 2)$ of the fundamental frequency on the axial compressive load $\bar{P}$ for selected values of the pretwist angle β (deg). The box-beam is characterized by $R = 0{\cdot}5$, $\theta = 0°$; ——, $\bar{\omega}_1$; – – –, $\bar{\omega}_2$.

Figure 7–11 depict the variation of the non-rotating lower and upper branches $(\bar{\omega}_i (\equiv \omega_i/\hat{\omega}_1 (i = 1, 2)$ of the fundamental frequency versus the normalized axial load, $\bar{P} (\equiv P/\hat{P}_{cr})$ for selected pretwist, ply-angles and cross-section R parameters. Herein $\hat{\omega}_1$ and $\hat{P}_{cr} (\equiv P_{cr} L^2/a^p_{33})$ denote the normalizing fundamental frequency and the buckling load,

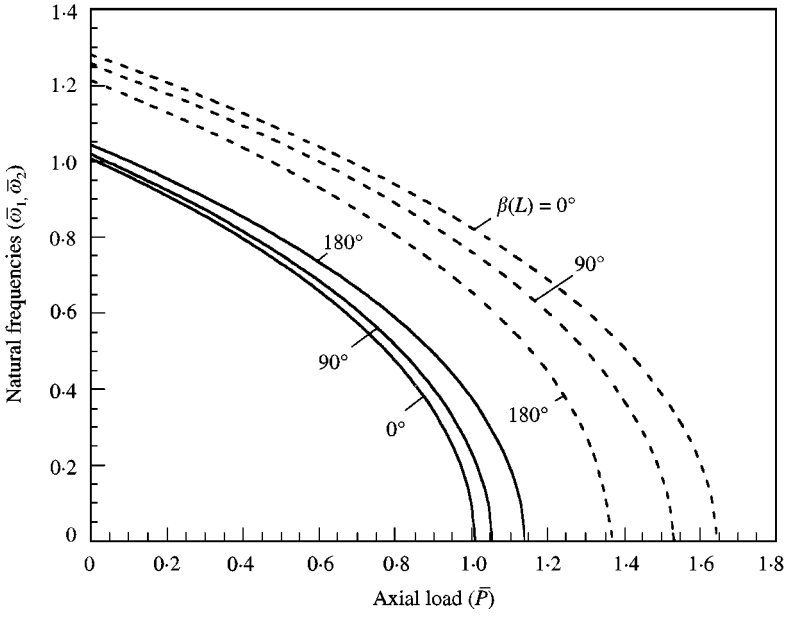

Figure 10. The counterpart of Figure 9 for the ply-angle $\theta = 45°$; ——, $\bar{\omega}_1$, – – –, $\bar{\omega}_2$.

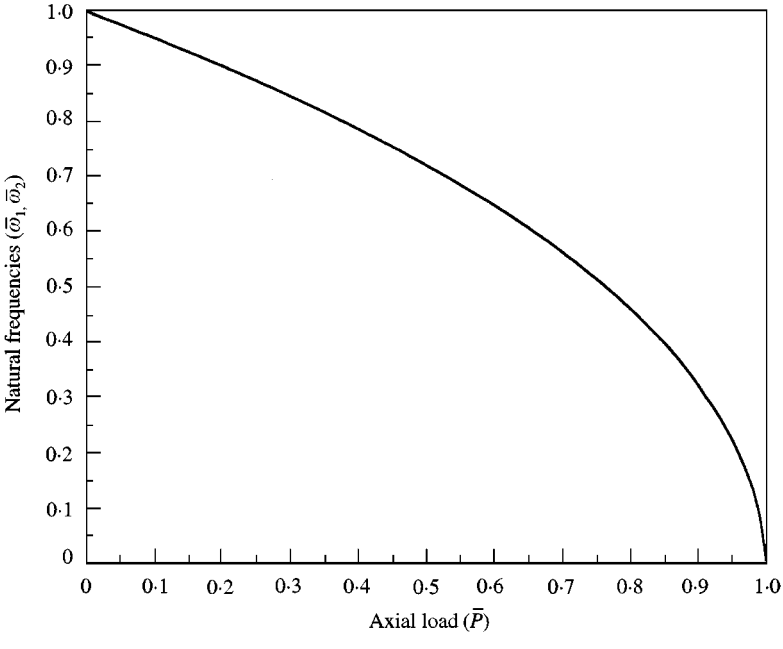

Figure 11. Dependence of the fundamental frequency on the compressive axial load for selected values of the pretwist angle, $\beta = 0°$, 45°, 90°, 135°, 180°. Herein the box-beam is characterized by $R = 1$, $\theta = 0°$, $\Omega = 0$.

respectively, correspond to $\bar{\Omega} = 0$, $\theta = 0$, $R = 1$ and $\beta = 0$, and have the values: $\hat{\omega}_1 = 164{\cdot}73$ rad/s, $\hat{P}_{cr} = 2{\cdot}43$, whereas $a^p_{33} = 2{\cdot}134 \times 10^8$ lb in^2.

From these plots it can be remarked that with the increase of the axial compressive load, the frequencies are decreasing. The value of the axial (normalized) load for which the

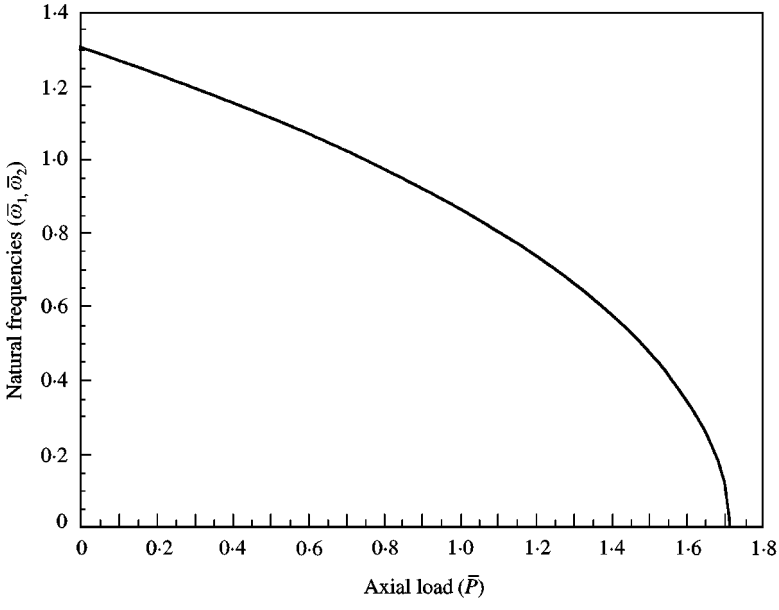

Figure 12. The counterpart of Figure 11 for $\theta = 45°$, $\beta(L) = 0°, 90°, 180°$.

frequency vanishes constitutes the critical (buckling) axial compressive load. With the increase of the pretwist angle, for the same compressive load, whereas the eigenfrequencies associated with the lower branch increases, those associated with the second one decrease. As a result, a beam featuring larger pretwist angles can sustain larger compressive edge loads before the occurence of buckling. For values the cross-section parameter R approaching 1, it becomes apparent that the frequency–load interaction curves associated with the lower and upper branches approach each other and for $R = 1$ these merge together. The results in these figures also reveal that the cross-section parameter R and the ply-angle θ can play an important role towards enhancing the behavior of the structure by increasing independently, each of these, the natural frequencies and the buckling load.

In contradistinction with the trend occurring in the case $R \neq 1$, for $R = 1$, the results displayed in Figures 11 and 12 reveal that the pretwist angle does not play any role on frequency–load interaction. On the other hand, the results of these plots outline once more the beneficial effect of the ply-angle on both eigenfrequency and buckling load.

Figure 13 depicts the lowest normalized buckling load versus the pretwist angle, for selected values R of the cross-section beam. The results show an expected result, namely that for $R = 1$, the buckling load is not affected by the pretwist angle. However, for the case $R \neq 1$, the buckling load increases as the pretwist increases and the cross-section parameter R decreases. These conclusions are similar to those in references [9, 10] obtained for a solid beam via the assumed-mode approximation, and the FEM, respectively.

9. CONCLUSIONS

An analytical study devoted to the mathematical modelling of spinning thin-walled beams featuring pretwist and experiencing bending–bending coupled motion has been presented. The numerical illustrations have revealed that the pretwisted spinning thin-walled beams can lose their stability by divergence and flutter. In addition to the

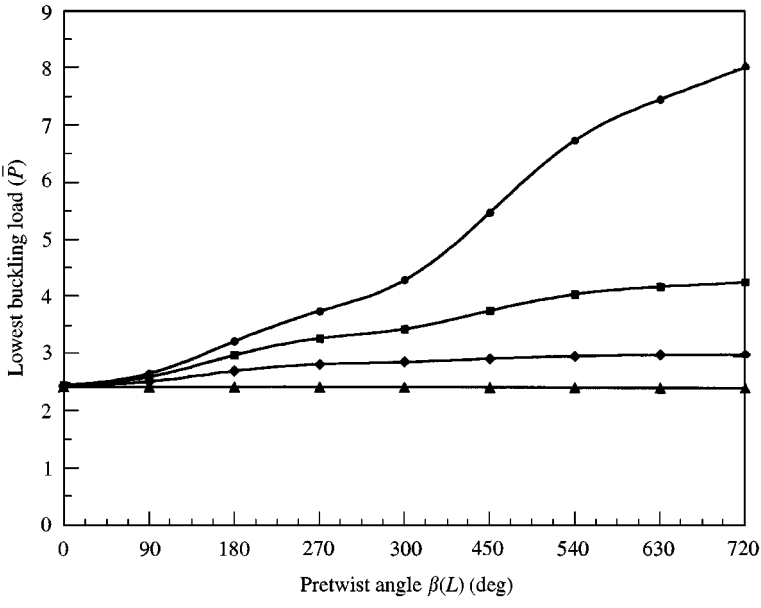

Figure 13. Variation of the lowest buckling load with the pretwist angle β (deg) for selected values of the cross-section beam parameter R, ($\theta = 45°$, $\Omega = 0$). —●—, $R = 0{\cdot}25$; , —■—, $R = 0{\cdot}5$; —◆—, $R = 0{\cdot}75$; —▲—, $R = 1$.

findings reported in references [33–36] revealing that flutter instability can occur in a *loaded* spinning beam, here, the results show that this instability can occur in an unloaded, but pretwisted beam, characterized by a cross-section parameter $R \neq 1$.

A number of conclusions related to the implications of pretwist on frequency–load interaction and on the buckling of thin-walled beams are also outlined. Although not explored in this paper, the tailoring technique used in reference [20], enabling one to enhance the frequency–load interaction and the dynamic behavior of spinning systems by extending their domains of stability towards larger spinning speeds and/or larger compressive loads, can also be applied to this case.

ACKNOWLEDGMENT

This work was supported in part by the Korea Science and Engineering Foundation (KOSEF 951-1002-030-2). This support is gratefully acknowledged by O. Song.

REFERENCES

1. H. F. BAUER 1980 *Journal of Sound and Vibration* **72**, 177–189. Vibration of a rotating uniform beam. Part I. Orientation in the axis of rotation.
2. P. L. HETHERINGTON, R. F. KRAUS and M. S. DARLOW 1990 *Journal of American Helicopter Society* **35**, 23–28. Demonstrations of a supercritical composite helicopter power transmission shaft.
3. C. W. BERT 1992 *Proceedings of the 6th Japan–U.S. Conference on Composite Materials*, 22–24 *June*, *Orlando*, *FL*, *U.S.A.* The effect of bending–twisting coupling on the critical speed of a drive shaft.
4. C. D. KIM and C. W. BERT 1993 *Composites Engineering* **3**, 633–643. Critical speed analysis of laminated composite hollow drive shaft.

5. C. W. BERT and C. D. KIM 1995 *Dynamics and Stability of Systems* **10**, 125–147. Dynamic instability of composite-material drive shaft subject to fluctuating torque and/or rotational speed.
6. G. M. ZHANG and S. G. KAPOOR 1997 *Journal of Engineering for Industry* **109**, 219–226. Dynamic modeling and analysis of the boring machining system.
7. E. I. RIVIN and H. KANG 1992 *International Journal of Machine Tools & Manufacture* **32**, 539–561. Enhancement of dynamic stability of cantilever tooling structures.
8. W. KIM, A. ARGENTO and R. A. SCOTT 1999 *Journal of Sound and Vibration* **226**, 125–147. Free vibration of a rotating tapered composite Timoshenko shaft.
9. M. L. CHEN and Y. S. LIAO 1991 *Journal of Sound and Vibration* **147**, 497–513. Vibrations of pretwisted spinning beams under axial compressive loads with elastic constraints.
10. C. L. LIAO and Y. H. DANG 1992 *Computers & Structures* **45**, 715–731. Structural characteristics of spinning pretwisted orthotropic beams.
11. C. P. FILIPICH, M. J. MAURIZI and M. B. ROSALES 1987 *Journal of Sound and Vibration* **116**, 475–482. Free vibrations of a spinning uniform beam with ends elastically restrained against rotation.
12. J. W.-Z., ZU and R. P. S. HAN 1992 *Journal of Applied Mechanics, Transactions of ASME* **59**, 197–204. Natural frequencies and normal modes of a spinning Timoshenko beam with general boundary conditions.
13. J. W. ZU and J. MELIANSON 1998 *Journal of Applied Mechanics, Transactions of ASME* **65**, 770–772. Natural frequencies and normal modes for damped spinning Timoshenko beam with general boundary conditions.
14. A. ZOHAR and J. ABOUDI 1973 *International Journal of Mechanical Scinces* **15**, 269–278. The free vibrations of a thin circular finite rotating cylinder.
15. S. C. JUANG and W. SOEDEL 1988 *Journal of the Acoustical Society of America* **84**, 275–285. On the forced vibration of simply supported rotating cylindrical shells.
16. O. RAND and Y. STAVSKY 1991 *International Journal of Solids and Structures* **28**, 831–843. Free vibration of spinning composite cylindrical shells.
17. L. HUA and K. Y. LAM 1998 *International Journal of Mechanical Sciences* **40**, 443–459. Frequency characteristics of a thin rotating cylindrical shell using the generalized differential quadrature method.
18. K. Y. LAM and L. HUA 1997 *International Journal of Solids and Structures* **34**, 2183–2197. Vibration analysis of a rotating circular conical shell.
19. K. R. SIVADAS 1995 *Journal of Sound and Vibration* **180**, 99–109. Vibration analysis of pre-stressed rotating thick circular conical shell.
20. O. SONG and L. LIBRESCU 1997 *Journal of Sound and Vibration* **204**, 477–494. Anisotropy and structural coupling on vibration and instability of spinning thin-walled beams.
21. A. ROSEN 1991 *Applied Mechanics Reviews* **44**, 483–575. Structural and dynamic behavior of pretwisted rods and beams.
22. O. SONG and L. LIBRESCU 1993 *Journal of Sound and Vibration* **167**, 129–147. Free vibration of anisotropic composite thin-walled beams of closed cross-section contour.
23. L. LIBRESCU and O. SONG 1992 *Composite Engineering* **2**, 497–512. On the static Aeroelastic tailoring of composite aircraft swept wings modeled as thin-walled beam structures. (Special issue: Use of composites in rotorcraft and smart structures).
24. A. GJELSVIK 1991 *The Theory of Thin Walled Bar*. New York: John Wiley and Sons.
25. L. LIBRESCU 1975 *Elasto-Statics and Kinetics of Anisotropic and Heterogeneous Shell-Type Structures*. Leyden, The Netherlands: Noordhoff International Publishers.
26. K. BHASKAR and L. LIBRESCU 1995 *International Journal of Engineering Science* **33**, 1331–1344. A geometrically non-linear theory for laminated anisotropic thin-walled beams.
27. L. MEIROVITCH 1997 *Principles and Techniques of Vibrations* Englewood Cliffs, NJ. Prentice Hall.
28. B. DAWSON 1968 *Journal of Mechanical Engineering Science* **10**, 381–386. Coupled bending–bending vibration of pretwisted cantilever blading treated by the Rayleigh–Ritz energy method.
29. O. TEKINALP and A. G. ULSOY 1989 *Journal of Vibration, Acoustics, Stress and Reliability in Design, Transactions of ASME* **111**, 148–154. Modeling and finite element analysis of drill bit vibrations.
30. M. ANLIKER and B. A. TROESCH 1963 *Zeitschrift für Agewandte Mathematics und Physics* (*ZAMP*) **14**, 218–236. Theory of lateral vibrations of pretwisted rods.
31. H. A. SLYPER 1962 *Journal of Mechanical Engineering Science* **4**, 365–379. Coupled bending vibrations of pretwisted cantilever beams.

32. M. SABUNCU 1985 *AIAA Journal* **23**, 1424–1430. Coupled vibration analysis of blades with angular pretwist of cubic distribution.
33. R. C. SHIEH 1971 *International Journal of Non-Linear Mechanics* **5**, 495–509. Energy and variational principles for generalized (gyroscopic) conservative problems.
34. R. C. SHIEH 1982 *Journal of Applied Mechanics, Transactions of ASME* **49**, 191–196. Some principles of elastic shaft stability including variational principles.
35. K. HUSEYIN and R. H. PLAUT 1974–1975 *Journal of Structural Mechanics* **3**, 163–177. Transverse vibrations and stability of systems with gyroscopic forces.
36. K. HUSEYIN and R. H. PLAUT 1975 *IUTAM Symposium, Lyngby, Denmark, August* 12–16, 1974, 182–205. Berlin: *Springer-Verlag*. Divergence and flutter boundaries of systems under combined conservative and gyroscopic forces.

APPENDIX A: STIFFNESS AND MASS TERMS

The expressions of stiffness quantities $a_{ij}(=a_{ij})$ *and mass terms* b_i intervening in equations (10) and (12)–(14) are

$$a_{22}=m^2a^p_{22}+n^2a^p_{33}-2mna^p_{23},\qquad a_{23}=mn[a^p_{22}-a^p_{33}],$$
$$a_{25}=m^2a^p_{25}-n^2a^p_{34}+mn[a^p_{24}-a^p_{35}],\qquad a_{33}=m^2a^p_{33}+n^2a^p_{22}+2mna^p_{23},$$
$$a_{34}=m^2a^p_{34}-n^2a^p_{25}+mn[a^p_{24}-a^p_{35}],\qquad a_{44}=m^2a^p_{44}+n^2a^p_{55}+2mna^p_{45},$$
$$a_{45}=mn[a^p_{44}-a^p_{55}],\qquad a_{52}=m^2a^p_{52}-n^2a^p_{43}+mn[a^p_{42}-a^p_{53}],$$
$$a_{55}=m^2a^p_{55}+n^2a^p_{44}+2mna^p_{54},\qquad b_1=b^p_1,\ b_4=n^2b^p_5+m^2b^p_4+2mnb^p_6,$$
$$b_5=m^2b^p_5+n^2b^p_4-2mnb^p_6,\qquad b_6=mn[b^p_5-b^p_4],\ b_{13}=mn[b^p_{14}-b^p_{15}],$$
$$b_{14}=m^2b^p_{14}+n^2b^p_{15}-2mnb^p_{13},\qquad b_{15}=m^2b^p_{15}+n^2b^p_{14}-2mnb^p_{13}.$$

In these expressions $m(z)=\cos\beta$, $n(z)=\sin\beta$, while the quantities affected by the superscript p are associated with the beam cross-section referred to the principal axes (x^p, y^p).

The expressions of stiffness and mass terms referred to the principal axes are supplied next:

$$a^p_{22}=\oint(K_{11}x^2+K_{44}(\mathrm{d}y/\mathrm{d}s)^2)\,\mathrm{d}s \quad \rightarrow \text{chordwise bending (lag) stiffness } [F-L^2],$$

$$a^p_{25}=\oint x(\mathrm{d}y/\mathrm{d}s)K_{12}+K_{24}(\mathrm{d}y/\mathrm{d}s)^2)\,\mathrm{d}s \quad \rightarrow \text{chordwise bending (lag)—flapwise transverse shear coupling stiffness } [F-L],$$

$$a^p_{33}=\oint(K_{11}y^2+K_{44}(\mathrm{d}x/\mathrm{d}s)^2)\,\mathrm{d}s \quad \rightarrow \text{flexural (flap) stiffness } [F-L^2],$$

$$a^p_{34}=\oint y(\mathrm{d}x/\mathrm{d}s)K_{12}+K_{24}(\mathrm{d}x/\mathrm{d}s)^2)\,\mathrm{d}s \quad \rightarrow \text{flexural (flap)—chordwise transverse shear coupling stiffness } [F-L],$$

$$a^p_{44}=\oint(K_{22}(\mathrm{d}x/\mathrm{d}s)^2+A_{44}(\mathrm{d}y/\mathrm{d}s)^2)\,\mathrm{d}s \quad \rightarrow \text{chordwise transverse shear stiffness } [F],$$

$$a^p_{55}=\oint(K_{22}(\mathrm{d}y/\mathrm{d}s)^2+A_{44}(\mathrm{d}x/\mathrm{d}s)^2)\,\mathrm{d}s \quad \rightarrow \text{flapwise transverse shear stiffness } [F],$$

$$a_{24}^p = \oint [x(\mathrm{d}x/\mathrm{d}s)K_{12} + (\mathrm{d}x/\mathrm{d}s)(\mathrm{d}y/\mathrm{d}s)K_{24}]\,\mathrm{d}s \rightarrow \begin{array}{l}\text{chordwise bending}\\ \text{chordwise transverse shear,}\\ [F-L]\end{array}$$

$$a_{35}^p = \oint [y(\mathrm{d}x/\mathrm{d}s)K_{12} + (\mathrm{d}x/\mathrm{d}s)(\mathrm{d}y/\mathrm{d}s)K_{24}]\,\mathrm{d}s \rightarrow \begin{array}{l}\text{flapwise bending}\\ \text{flapwise transverse shear,}\\ [F-L]\end{array}$$

$$(b_1^p,\ b_4^p,\ b_5^p,\ b_6^p) = \oint m_0(1,\ y^2,\ x^2,\ xy)\,\mathrm{d}s,$$

$$(b_{13}^p,\ b_{14}^p,\ b_{15}^p) = \oint m_2\left(\frac{\mathrm{d}x}{\mathrm{d}s}\frac{\mathrm{d}y}{\mathrm{d}s},\ \left(\frac{\mathrm{d}x}{\mathrm{d}s}\right)^2\left(\frac{\mathrm{d}y}{\mathrm{d}s}\right)^2\right)\mathrm{d}s,$$

where $(m_0,\ m_2) = \sum_{k=1}^{N} \int_{h_{(k)}} \rho_{(k)}(1, n)^2\,\mathrm{d}n$ and $\oint(\cdot)\,\mathrm{d}s$ denotes the integral around the circumference of the mid-line cross-section of the beam. K_{ij} intervening in the expressions of a_{ij}^p are local stiffness quantities defined in reference [22].